Velocity structure of the upper mantle discontinuities beneath North America from waveform inversion of broadband seismic data using a genetic algorithm

F. A. Neves, S. C. Singh, Keith Priestley

JOURNAL OF GEOPHYSICAL RESEARCH, VOL. 106, NO. B10, PAGES 21,883–21,895, OCTOBER 10, 2001

Velocity structure of the upper mantle discontinuities beneath North America from waveform inversion of broadband seismic data using a genetic algorithm

F. A. Neves, S. C. Singh,[1] and Keith Priestley

Bullard Laboratories, University of Cambridge, Cambridge, England, UK

Abstract. We present a velocity structure of the mantle discontinuities beneath the United States from a full waveform inversion of broadband seismic data. The data consist of 10 moderate earthquakes in the western United States that were recorded on 13 broadband seismometers across the United States operated by the U. S. National Seismic Network. A total of 36 seismograms with distance ranging from 1150 to 2700 km were used. A full waveform inversion based on two-dimensional modeling and one-dimensional inversion methods using a genetic algorithm was adopted. The inversion method is objective, provides error bounds on the model, and does not require any a priori information about these discontinuities. We find that the upper discontinuity is ~10 km thick, from 395 to 405 km, where the velocity increases from 8.80 to 9.15 km s^{-1} with a velocity gradient of 0.035 s^{-1}. The lower discontinuity is ~5 km thick, occurring over a depth range of 650-655 km, where the velocity increases from 10.20 to 10.70 km s^{-1}. Our results are in agreement with previous studies of the lower discontinuity but do not agree for a sharp (< 5 km) upper mantle discontinuity.

1. Introduction

Many of the fundamental questions concerning the chemistry and dynamics of the mantle hinge on the physical properties at the 410- and 660-km discontinuities, where phase changes occur due to the increase of pressure with depth. The wide majority of previous seismological studies have used trial and error methods of forward modeling to determine the depth and sharpness of these discontinuities. They have used either short-period data [*Benz and Vidale*, 1993; *Vidale et al.*, 1995] or long-period data [*Shearer*, 1996; *Dey et al.*, 1993; *Burdick and Helmberger*, 1978; *Burdick*, 1981]. These discontinuities have also been studies using very long refraction profiles [*Priestley et al.* 1994; *Neves et al.*, 1996]. The results from most of these studies are consistent for the 660-km discontinuity, but there is a large variation in the results for the sharpness of the 410-km discontinuity. For example, *Benz and Vidale* [1993] suggest that the "410" discontinuity should be < 5 km thick, whereas *Bowman and Kennett* [1990] suggest that it should be 20 km thick. *Neves et al.* [1996] proposed a two-step discontinuity, an upper 5-10 km thick high-velocity gradient zone below which there is a 15-20 km thick low-velocity gradient. On the other hand, high-pressure mineral physics studies [*Katsura and Ito*, 1989; *Akaogi et al.*, 1989; *Akaogi and Ito*, 1993; *Bina and Wood*, 1987; *Helffrich and Wood*, 1996] suggest the 410-km discontinuity to be 8-19 km thick and the 660-km discontinuity to be 1-10 km thick.

In the last decade, there has been a significant increase of broadband seismic networks. Broadband data are suitable for waveform analysis which provides more stringent constraints on the velocity structure of the Earth. Waveform analysis can be carried out using either a trial and error forward modeling method or an inversion method. Although the trial and error modeling provides some insight about the velocity structure, it is based on qualitative human judgement, and thus there is no way to assess the uncertainty of the resulting models. Waveform inversion is an objective approach and provides uncertainty for the derived model. However, the waveform inversion is a nonlinear problem, particularly for critically reflected data usually observed from the mantle discontinuities. We present a nonlinear waveform inversion method based on a genetic algorithm for optimization. The method was applied to broadband data collected between June 1992 and September 1994 on 12 U. S. National Seismic Network (USNSN) stations across the United States.

[1] Also at Laboratoire de Géosciences Marines, Institut de Physique du Globe de Paris, France.

Paper number 2001JB000198.
0148-0227/01/2001JB000198$09.00

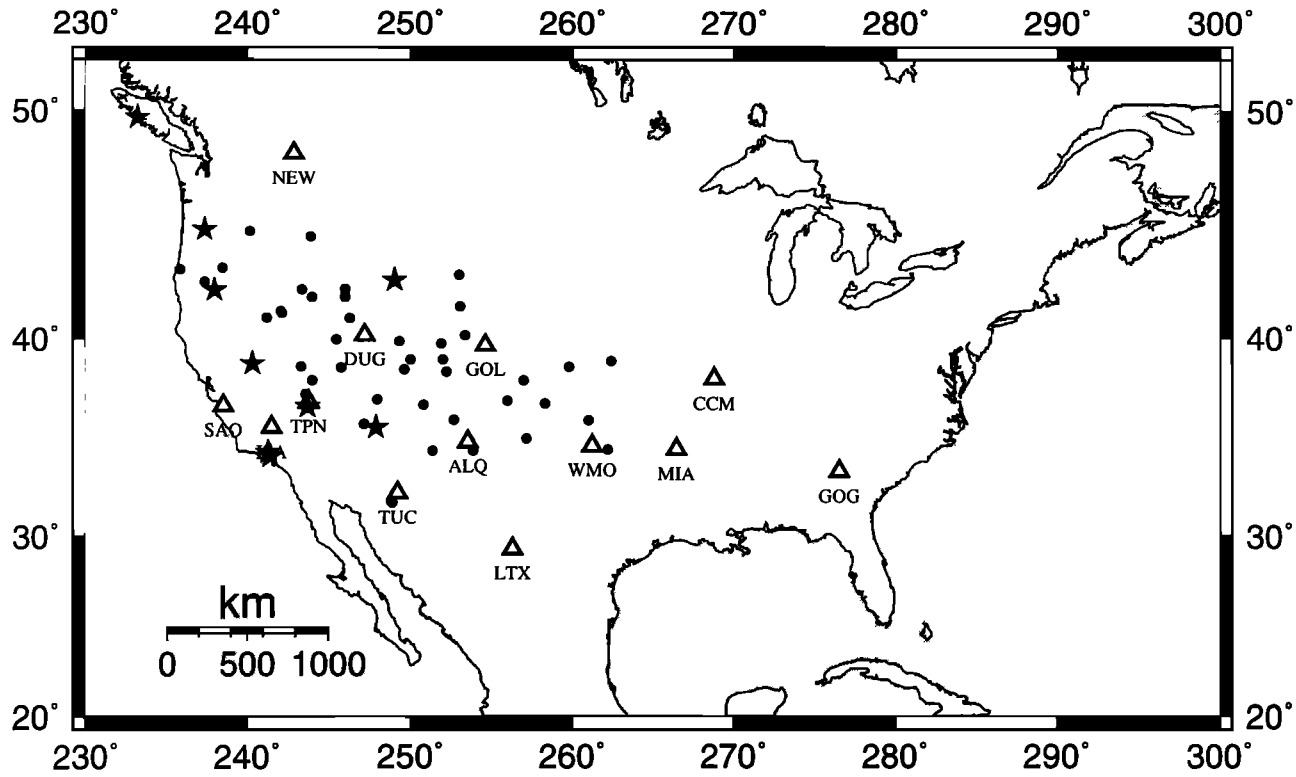

Figure 1. Map of North America showing the locations of earthquakes (stars), USNSN stations (open triangles), and common midpoints (solid dots) between earthquakes and stations.

2. Broadband Seismic Data

We used digital seismograms from 12 recording instruments of the United States National Seismograph Network (USNSN) for 10 moderate earthquakes ($m_b >$ 5.3) in the western United States (Figure 1, Table 1 and Table 2). The USNSN seismographs have Guralp CMG-3 seismometers with a frequency bandwidth of 0.03 to 30 Hz. Because of the type and quality of the instrumentation and the network distribution, the USNSN has a unique research potential for studies on regional and continental scales. The moderate earthquakes studied here are sufficiently energetic to illuminate the transition zone structure but small enough that the source is relatively simple. Thirty-six seismograms in the distance range 1150-2700 km for 10 earthquakes were chosen for analysis, all of which show clear P wave arrivals from the upper mantle transition zone. The midpoint (turning point) locations of the source-receiver pairs are roughly aligned in NW-SE direction (Figure 1). Earthquake source parameters were taken from the Harvard centroid moment tensor (CMT) catalogue (Table 1). The source time function was parameterized as an isosceles triangle [*Nábělek*, 1984] of duration $2dt$, where dt is the half duration provided by the Harvard CMT catalogue. This kind of parameterization leads to synthetic seismograms which contain a spectra decay of w^{-2} at high frequencies, which is typical for earthquakes [*Nábělek*, 1984]. Frequency analysis of the data indicates that the useful bandwidth is between 0.05 and 2.0 Hz.

Table 1. Sources Parameters Given by the CMT Solution

Earthquake	Latitude, °N	Longitude, °E	Depth, km	Magnitude, m_b
920628	34.20	243.56	1.0	6.2
920629	36.71	243.61	9.0	5.6
930325	45.04	237.39	21.0	5.5
930429	35.61	247.89	10.0	5.5
930921	42.31	237.99	11.0	5.7
940103	49.72	233.23	19.0	5.4
940117	34.21	241.46	18.0	6.4
940118	34.38	241.30	11.0	5.4
940203	42.76	249.13	8.0	5.4
940912	38.82	239.34	14.0	5.4

Table 2. Location of Seismographs

Symbol	Latitide, °N	Longitude, °W	Town	State
ALQ	34.943	73.54	Albuquerque	New Mexico
TPN	36.929	63.78	Topopah Springs	Neveda
CCM	38.056	88.75	Cathedral Cavel	Missouri
DUG	40.195	67.19	Dugway	Utah
GOG	33.411	96.53	Godfrey	Georgia
GOL	39.700	74.63	Golden	Colorado
ISA	35.663	61.53	Isabella	California
LTX	29.334	76.33	Lajitas	Texas
MIA	34.546	86.43	Mount Ida	Arkansas
NEW	48.263	62.88	Newport	Washington
SAO	36.765	58.56	San Andreas Observatory	California
TUC	32.31	69.22	Tucson	Arizona
WMO	34.738	81.22	Wichita Mountains	Oklahoma

3. Nonlinear Global Waveform Inversion

Our inversion method consists of two steps: (1) travel time inversion and (2) a full waveform inversion. The travel time inversion allows the determination of large-scale velocity structure, whereas the waveform inversion provides information of the detailed velocity structure. The forward calculation is carried out using Maslov asymptotic theory [*Chapman and Drummond*, 1982]. This method allows the efficient computation of travel times and waveforms in two-dimensional (2-D) smoothly varying media, which is valid at caustics and provides accurate amplitudes. One of the advantages of the Maslov method is that it does not require any free parameters, unlike the Gaussian beam method [*Červený et al.*, 1982], which requires the Gaussian beam width for different types of rays. Therefore the former method is very suitable for a global inversion. Since the reflections from the upper mantle arrive at large distances (1000-3000 km), the Earth's surface curvature is important. Although this is done in two dimensions, we use a 1-D Earth flattening transformation [*Chapman*, 1973], which is adequate for this narrow range of distances considered. The method also takes into account anelastic attenuation.

Inversion consists of minimizing a misfit function, which describes the mismatch between observed and synthetic data. The travel time misfit is defined as

$$\phi_{tt} = \frac{1}{n}\sum_{i=1}^{n}\frac{(t_i^d - t_i^s)^2}{\Delta t_i^2}, \tag{1}$$

where t_i^d and t_i^s are the observed and theoretical (synthetic) travel times, Δt_i is an estimate of the uncertainty (error) of the time-picking process, and the summation is performed over the number of picked arrivals, n. In addition to approximate normalization, Δt_i achieves the desired result of downweighting the contribution to the misfit function of travel time picks with larger errors.

The choice of a robust and fair waveform misfit function is more complicated than that of the travel time case. The misfit function must replicate the inherent judgement of the "seismologist's eye." At the same time, it must be applicable to data of varying quality, and also to be fair, it must ensure that high-amplitude arrivals do not dominate lower amplitude arrivals. Our chosen waveform misfit function is defined in the frequency domain as [*Cary*, 1988]

$$\phi_{wf} = \frac{\sum_{j,k,l}[d_{j,k}\hat{A}(\omega_l)\hat{d}(\omega_l, x_{j,k}) - c d_{j,k} P_s(\omega_l, x_{j,k})]^2}{\sum_{j,k,l}[d_{j,k}\hat{A}(\omega_l)\hat{d}(\omega_l, x_{j,k})]^2}, \tag{2}$$

where $\hat{d}(\omega_l, x_{j,k})$ is the lth frequency component of the jth observed seismogram (each seismogram may have more than one modeled phase, indicated by the k index), having an offset of $x_{j,k}$. $P_s(\omega_l, x_{j,k})$ is the corresponding component in the synthetic data. The Maslov algorithm yields the synthetic seismogram response P_s in the frequency domain, with implicit smoothing by a fourth-order box-car function. The operator $\hat{A}$ is applied to the observed data to mimic this smoothing. In the frequency domain,

$$\hat{A}(\omega) = \mathrm{sinc}^4(\frac{\omega}{\omega_N}), \tag{3}$$

where ω_N is the Nyquist frequency (π/dt, for sample interval of dt); $d_{j,k}$ are range-dependent weights, computed from the observed data such that each seismogram contributes equally to the total misfit. Unfortunately, this weighting operation may result in the loss of relative amplitude information from one seismogram to the next. Nevertheles, this is considered preferable to domination of the misfit function by high-amplitude near-offset events. The velocity structure of the deep subsurface, resolved by lower-amplitude far-offset events, would then be well constrained, and this is the part of the model space in which we are most interested. Finally, the c factor in equation (2), defining the absolute scaling of the synthetics is given by

$$c = \frac{1}{n} \sum_{j,k} \frac{E\{d(\tau_{j,k}, x_{j,k})\}}{\max\{E[P_s(t, x_{j,k})]\}}, \quad (4)$$

where $\tau_{j,k}$ satisfies

$$E\{P_s(\tau_{j,k})\} = \max\{E[P_s(t, x_{j,k})]\}. \quad (5)$$

E is the modulus of the complex trace, or envelope function, and the summation is over all the modeled arrivals (offset index j, phase index k); $\tau_{j,k}$ is defined as the time in the synthetic seismogram at which the envelope function is a maximum. This method of determining the global scaling factor matches the seismologist's eye [*Cary*, 1988] since it is insensitive to small time misalignments of the observed and synthetic waveforms.

Waveform inversion of critically reflected data is a nonlinear problem. Therefore we employ a global search algorithm (genetic algorithm) to obtain the best fitting model. The genetic algorithm (GA) is based on the process of natural selection. It works with a population of models, instead of with individual models. The GA involves three processes: selection, crossover, and mutation [*Goldberg*, 1989]. The initial population of models is chosen randomly. The selection process ensures that models with higher fitness (or lower misfit) have a better chance of being selected for future generations. The crossover process allows the exchange of different parts of pairs of models to create a new set of models, which allows the important part of different models to dominate the search process. In the mutation process, certain parts of models are changed randomly in order to allow the search to escape from any local minimum and sample broad region of the model space.

The purpose of the GA is to explore favourable regions of the model space when searching for the optimum model. Because of the presence of noise and the uncertainty in the time-picking process, many models satisfy the observed data equally well. Therefore the formal solution to the inverse problem consists of assigning probabilities to each of the recovered parameters. The a posteriori probability density (PPD) is estimated using a graph binning technique [*Frazer and Basu*, 1990; *Basu and Frazer*, 1990].

Assuming Gaussian errors in both travel times and waveforms, a model with misfit $\phi(\mathbf{m})$ is assigned a probability given by

$$\sigma(\mathbf{m}) = \frac{\exp\{\frac{-[\phi(\mathbf{m}) - \phi_{\min}]}{2\phi_\sigma^2}\}}{\sum_j \exp\{\frac{-[\phi_j(\mathbf{m}) - \phi_{\min}]}{2\phi_\sigma^2}\}}, \quad (6)$$

where ϕ_σ is the standard deviation of the distribution of misfit values and the summation is over all models within the current iteration which pass the traveltime test. The misfit of the best fitting model, $\phi_{\min}$, is subtracted from the misfit, ϕ, to enhance the influence of models close to the ultimate optimum model. The presence of noise and signal, which is not modeled, implies that the minimum misfit may not reach zero, particularly for the case of waveform inversion. The required $\phi_{\min}$ is the lowest misfit discovered during the entire GA run. A trial inversion establishes this value before repeating the GA to recover the correct PPDs. Graph binning technique is performed by assigning a bin (window) to each discrete value that each model parameter might take during the inversion process. Once a probability has been computed for a particular model, that value is summed into a bin corresponding to that model parameters. Dividing the value stored in each bin by the number of models contributing to that bin yields the normalized PPD, computed after the final iteration of the GA. This approach is different from that of *Sen and Stoffa* [1992], who also adapted *Frazer and Basu's* [1990] technique for use with GA. In normalizing the PPD, *Sen and Stoffa* [1992] use the total probability summed over all bins, rather than taking into account the number of models contributing to each discrete bin. As the number of iterations of the GA increases, this method results in PPDs which approximate delta functions (with small width arising from the crossover in the GA scheme). Clearly, the PPDs cannot be delta functions where the data are band-limited. The method used here does, at least, result in sensible PPDs, having reasonable (given path length and frequency content) width, although it does not have the rigor of the full error analysis which has been developed for the Monte Carlo technique [e.g., *Cary and Chapman*, 1988].

The estimated probability, $\sigma(\mathbf{m})$, is also used to compute a mean model,

$$\bar{\mathbf{m}} = \sum \mathbf{m}\sigma(\mathbf{m}), \quad (7)$$

where the summation is over all successful models in all iterations. Velocity-depth profiles presented in sections 4 and 5 show both the best (lowest misfit) model as well as the mean model.

4. A Priori Information

One can only extract a limited amount of information from 36 seismograms; therefore we focus our effort in determining a detailed 1-D velocity structure of the mantle discontinuities and assume that the crustal and upper mantle velocity structures are known. Figure 1 shows that the earthquakes are located in the tectonically active region of the western United States, whereas the seismographs are located in both the tectonically active and stable regions of North America. To account for the lateral velocity variation in the crust and upper mantle structure between these two regions, we have built a 2-D velocity structure by combining the velocity models S8 and T9 of *Burdick* [1981]; otherwise, E-W variations in the velocity structure would generate time delays at different ranges which would affect the depth and thickness estimates of transition zone discontinuities. Figure 2 shows velocity models S8 and T9; these models were determined by 1-D forward modeling that matched long-period seismograms with synthetic seismograms. Since velocity models S8 and T9 were derived

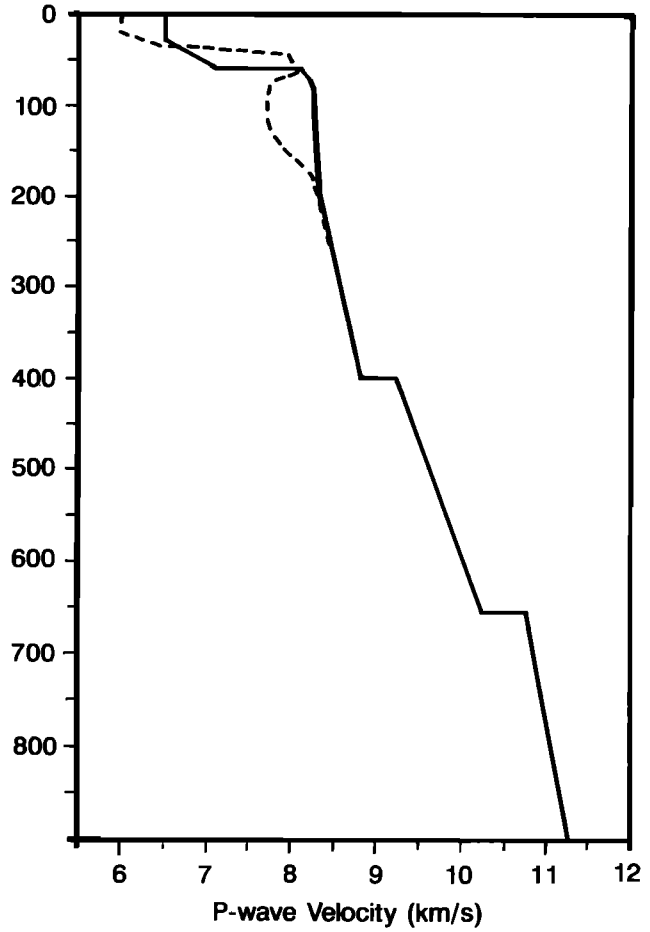

Figure 2. *P* wave velocity models for stable (S8, dashed line) and tectonic (T9, solid line) North American continental structure [*Burdick*, 1981]. The only differences in models occur above 250 km.

from long-period data, small-scale structures can not be resolved. The tectonic model T9 is a variant of the western U.S. velocity model T7 of *Burdick and Helmberger* [1978]. In model T9, the 410-km upper mantle discontinuity has been raised slightly (compared to velocity model T7). *Burdick and Helmberger* [1978] did not have any observations of reflections coming from the 410-km discontinuity so T7 was unconstrained with regard to this triplication branch. T9 has a well-developed low-velocity zone, which is appropriate for a tectonically active regions [*Helmberger*, 1973], but S8 has a thicker crust and no upper mantle low-velocity zone. Most of the lateral variations in these models occur above 250 km depth. These models show simple, sharp step-like velocity increases for the "410-km" and "660-km" discontinuities. S8 and T9 provide a good background velocity model for more detailed studies using data with a broader frequency bandwidth. We combined these two models to obtain a 2-D smooth model taking into account the area covered by the two geologically distinct regions. We refer to this combined velocity model as S8T9, which provides a smooth 2-D *P* wave velocity and attenuation across the United States. The parameters for the attenuation were taken from *Burdick and Helmberger* [1978] and *Burdick* [1981]. Because of inaccuracies regarding event location, source time function, and the widespread station distribution (which averages the mantle structures along the ray paths), lateral velocity variation in the upper mantle transition zone is not constrained by the data.

5. Travel Time Inversion

We have analyzed the USNSN data set in two ways. First, the seismograms of each earthquake are analyzed separately to give a local estimate of the transition zone structure. Second, we invert the 36 seismograms simultaneously to generate the best average velocity model. The same methodology discussed in section 3 was applied in both cases. The individual inversions will provide better estimates of the local velocity structure, whereas the collective inversion will provide a better estimate of the average velocity structure.

In the travel time inversion an initial population of velocity models was chosen randomly from within the velocity range $V_{S8T9} \pm 0.5$ km s^{-1}, where V_{S8T9} is a velocity for S8T9. The velocity deviation in this range is greater than the typical accuracy of $\pm$ 0.1 km s^{-1} provided by ordinary earthquake seismological studies. We imposed a positive velocity gradient at the transition zone discontinuities to avoid the presence of low-velocity zones at those depths; this constraint speeds up and improves the performance of the inversion algorithm. The chosen bounds allow sufficient variation of upper mantle velocities without allowing exceptionally high or low velocities in the model space definition. The velocity discretization value, dv, was set to 0.05 km s^{-1} for each layer. Because only the details of the velocity discontinuities at the upper mantle transition zones are sought, only the velocity in the vicinity of these discontinuities was allowed to vary; the model is fixed elsewhere. In total, 22 depth nodes were used, 14 for the 410-km discontinuity, 1 at the intermediate depth of 500 km, and 7 for the 660-km discontinuity. A linear interpolation was used to estimate the velocity between two consecutive depth node points. In order to resolve the two discontinuities the nodes were placed at every 5 km from 380 to 440 km and from 640 to 670 km. This node spacing was based on the highest resolution possible from the data. A node placed at 450 km in case the 410-km discontinuity was at 10 km. A large number (14) of nodes were necessary for this discontinuity in order to distinguish between sharp (5 km) and thick (35 km) models for the 410-km discontinuity.

The distance range (1400-3000 km) corresponds to the critical angle reflections from the two discontinuities. The travel times of the critically reflected arrivals mainly depend on the travel path, whereas the waveforms are controlled by the nature of the reflector. Any error in the background velocity will introduce a systematic time shift and will not significantly effect the

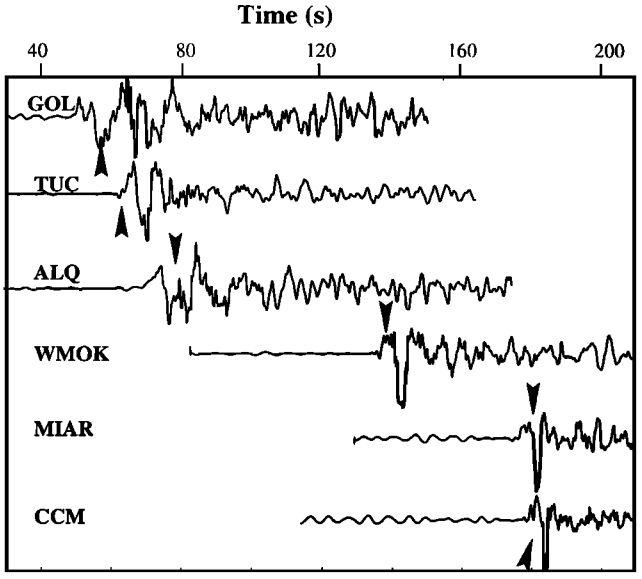

Figure 3. Raw data for 930921 event recorded at six different stations at distances ranging from 1427 km (GOL) to 2647 km (CCM). The main arrivals used in the inversion are marked by arrows. At near distances, reflections from the 410- and 660-km discontinuities arrive close to each other resulting in a complex waveform pattern. At large distance, reflection from the 660-km discontinuity is dominant. For the source mechanism and station azimuth, see Figure 6.

waveforms. The main arrivals were picked to an accuracy of 100 ms. Figure 3 shows that the main arrivals are energetic and the signal-to-noise ratio is high (over 100). The amplitudes of the Maslov synthetic seismograms are dictated by the density of turning rays arriving near a particular distance, i.e., the denser the rays, the higher the amplitude of the arrival. Travel times are computed by interpolation from the results of ray tracing a fan of 500 rays. The slowness of each ray within the fan is adaptively computed for each velocity model to ensure that a reasonable number of rays turn within the gradient zone between two neighboring nodes.

For the genetic algorithm the population size was 500, selection probability of 0.8, crossover probability of 0.8 and mutation probability of 0.05. Models failing the travel time test, that is, models leading to at least one synthetic arrival time outside the bounds of the picked arrival time, are assigned the same, large, penalizing misfit value of 10,000. The final travel time inversion is used to provide a pool of models from which to initiate the waveform inversion. To ensure a sufficiently large pool of models for the proposed waveform inversion, the travel time inversion was only halted after a minimum of 50 acceptable velocity models had been generated. In order to illustrate the improvement of the estimated velocity model that was achieved, the travel time inversion result for the 930429 event is presented (Figure 4).

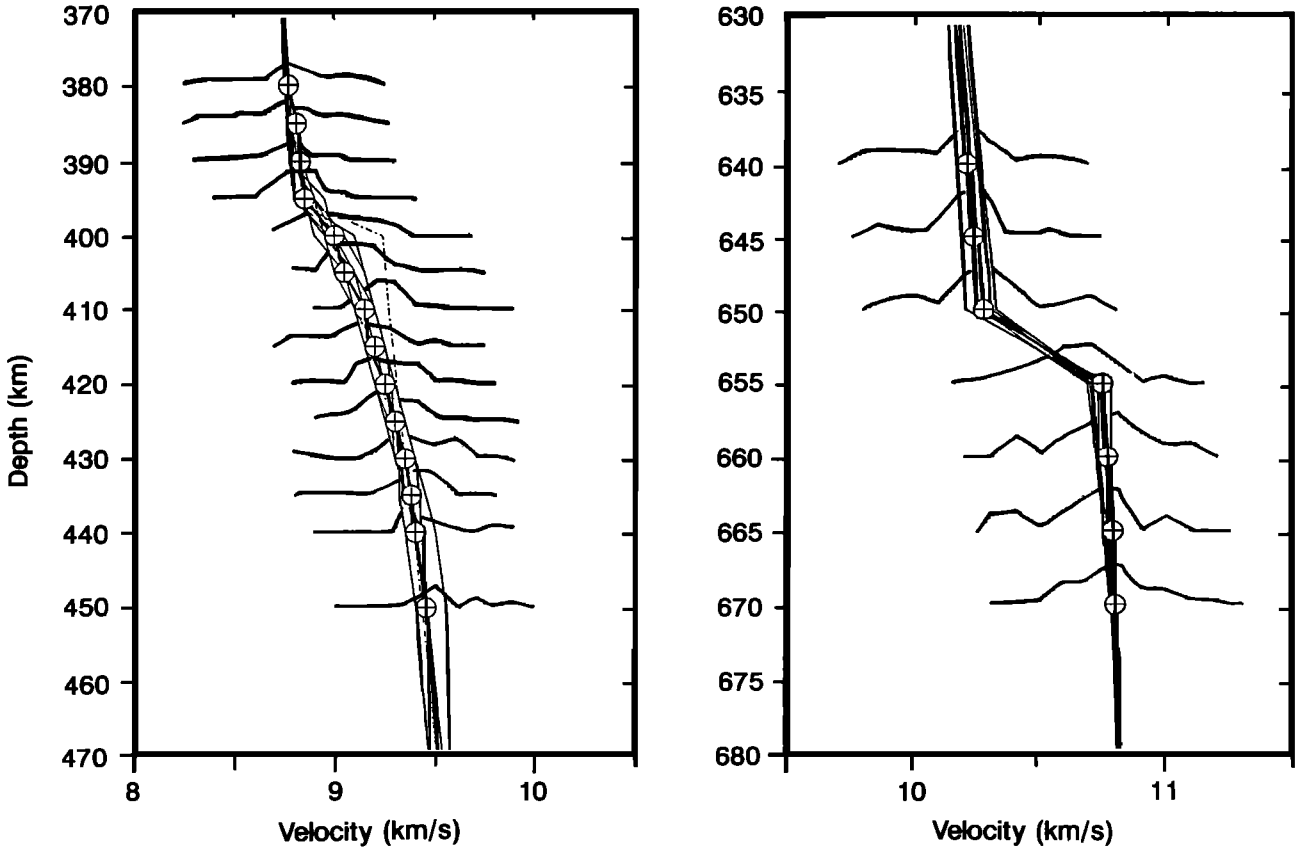

Figure 4. *P* wave velocity depth-function for the (left) 410-km and (right) 660-km discontinuities estimated by travel time inversion of the individual earthquake events, the best travel time fitting model (solid lines with circles), T9 [*Burdick*, 1981](dashed line), and the PPD for the velocity parameters (horizontal dashed lines).

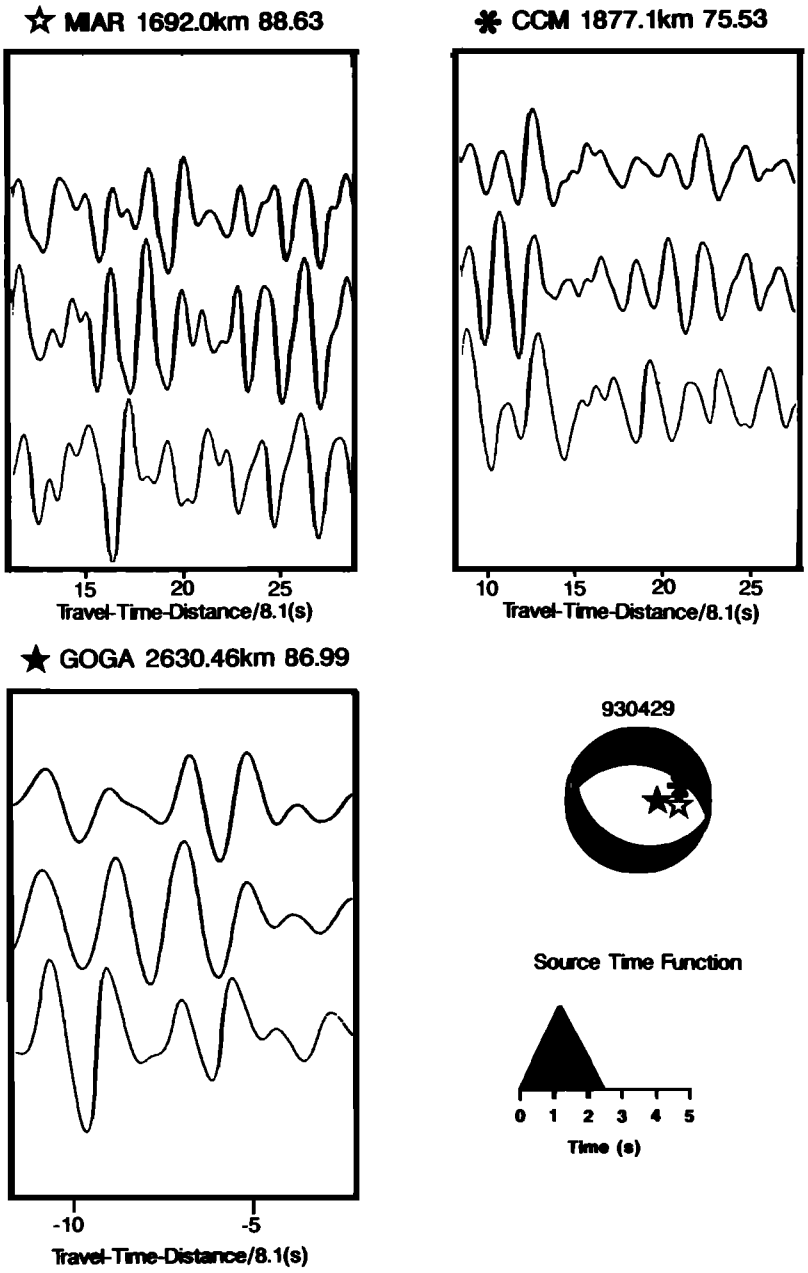

Figure 5. Comparison between data (top curve), synthetic seismograms obtained from the best traveltime fitting model (middle curve) and from Burdick's model (bottom curve) for event 930429. The station name, distance, and azimuth are shown above each panel. The source time function and the focal mechanism given by the CMT solution, with stations superimposed on the focal mechanism are given.

The final velocity model (thick solid line with crossed circles) and all the models from individual earthquakes (thin solid lines) are shown in Figure 4; seismograms computed from the final velocity model are shown in Figure 5. The travel time misfit of this best velocity model was 120 ms, comparable to the picking error of 100 ms.

6. Waveform Inversion

The waveform inversion of the USNSN data set was implemented with an initial population of 50 velocity models and with crossover and mutation probabilities equal to $P_c = 0.7$ and $P_m = 0.05$, respectively. These were obtained from preliminary tests on the data. The model space bounds and the vertical separation between depth nodes were the same ones used in the travel time inversion. The attenuation model used in computing the synthetic seismograms is from *Helmberger* [1973]. The waveform inversion was run for 500 iterations; however, we found that the misfit values did not change significantly after ~300 iterations, suggesting that a total of 500 iterations was sufficient to achieve convergence. The inversion for the whole data set required 120 min of CPU time on a Sparc-10 workstation.

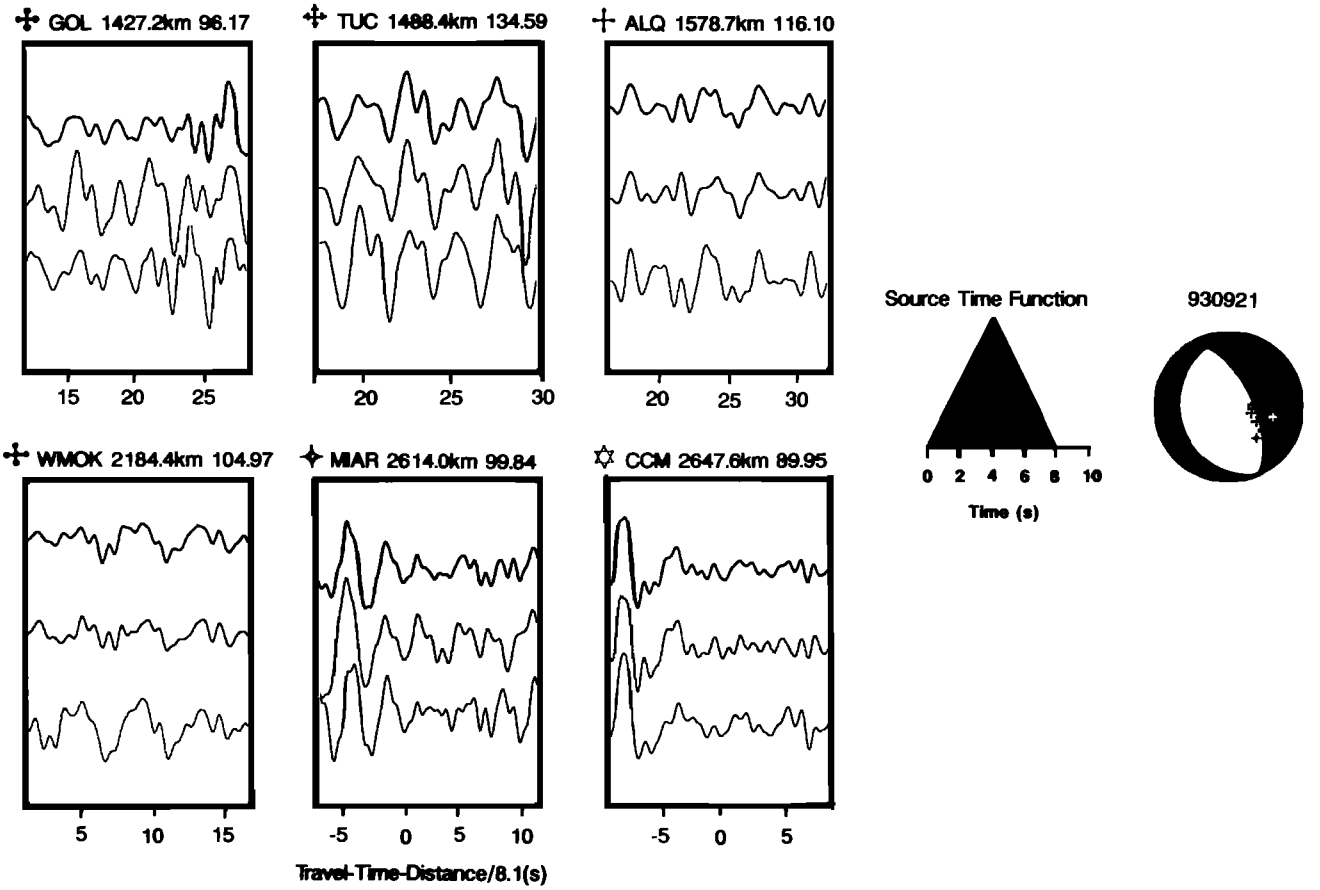

Figure 6. Comparison between data (top curve), synthetic seismograms obtained from the best waveform fitting model (middle curve) and from S8T9 (bottom curve) for event 930921. Format is the same as in Figure 5.

6.1. Individual Event Inversions

Although noise is high, the individual event inversions provide useful and reliable local 1-D velocity structure. In order to reduce the effect of noise we also invert all the events simultaneously. Here we only present the results for event 930921 for both cases. We have chosen event 930921 to illustrate the results because of the large number of stations and the high quality of the seismograms for this event. The results for all the other events are given by *Neves* [1996]. The misfits between the data and synthetic seismograms for individual events were between 0.5 and 0.7.

Event 930921 was recorded at six USNSN stations (GOL, TUC, ALQ, WMOK, MIA, and CCM) in the distance range 1427 to 2647 km. These seismograms show an irregular wave shape with several crustal and upper mantle phases. Figure 6 shows synthetic seismograms for the best fitting model. Both the data and the synthetic seismograms have been filtered in the same frequency bandwidth (0.05 to 2.0 Hz). Since observed waveforms vary significantly across nodal planes, the location of the seismic wave takeoff angle from each station is plotted on the focal sphere. This provides a simple check if a station is located near a nodal plane of the radiation pattern. This would explain some degree of mismatch between synthetic and observed seismograms. The waveform match between the synthetic seismogram and observed seismogram (Figure 6) is variable. Onset for all the stations (except GOL) is reasonably estimated from the best fitting velocity model, shown in Figure 7 and for velocity model S8T9. Note the better match provided by the best fitting model for station WMOK between 2 and 12 s and also for station ALQ between 18.5 and 27 s. A simple source mechanism (despite the relatively long 8-s time duration of the source) has helped to achieve this very good match. The relative amplitude among the phases on the observed seismogram is generally well predicted by the synthetic seismograms.

The best fitting velocity model for the 410-km discontinuity is slower than for S8T9 and indicates a lower gradient (0.025 s^{-1}) from 400-km depth (velocity of 8.90 km s^{-1}) to 405-km depth (velocity of 9.15 km s^{-1}). However, the PPDs curves are quite broad between 395 and 425 km depth, so that velocity model S8T9 for these depths cannot be ruled out. The best fitting velocity model for the 660-km discontinuity is very similar to that of S8T9: an estimated 5-km-thick transition zone (gradient of 0.010 s^{-1}) with velocity varying from 10.30 km s^{-1} at 650-km depth to 10.80 km s^{-1} at 655 km.

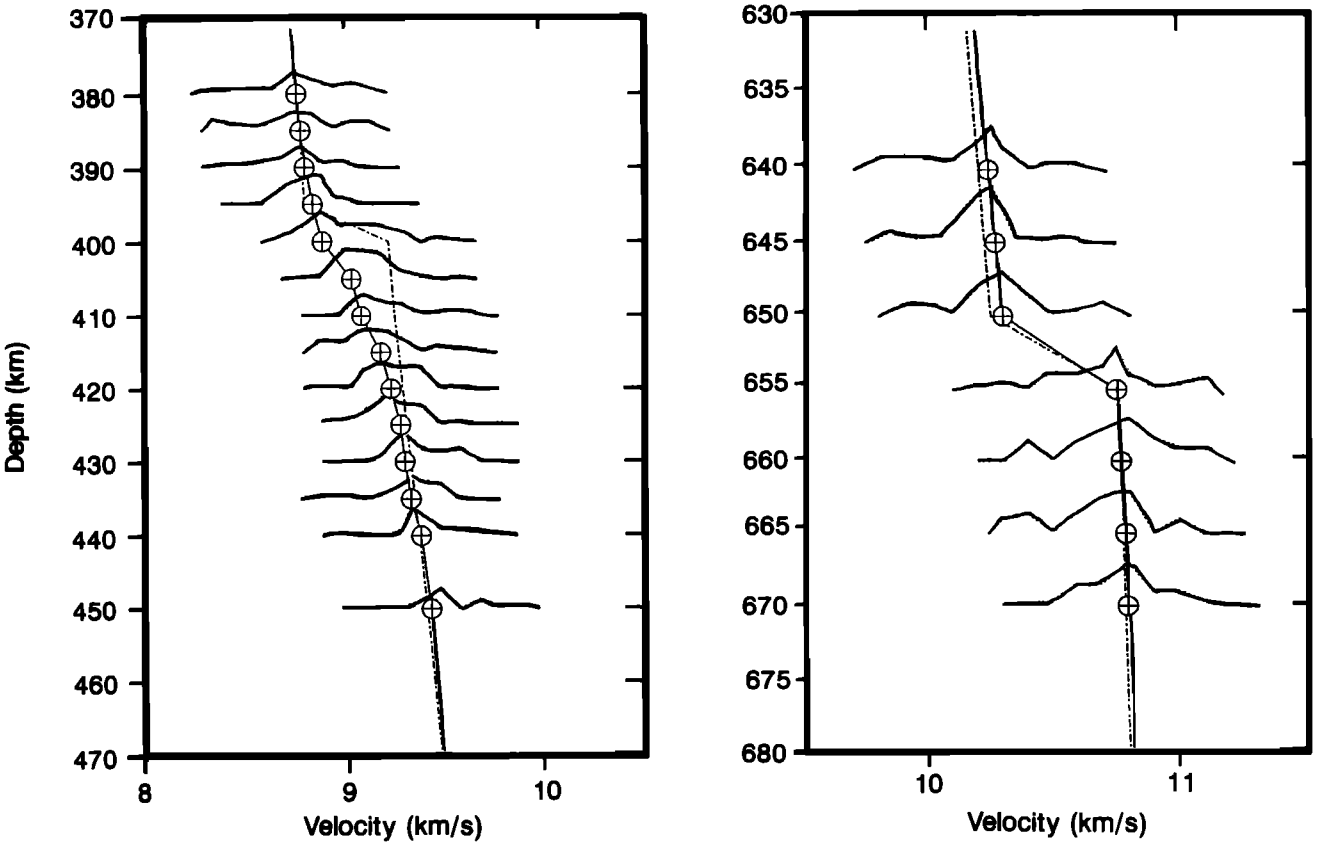

Figure 7. *P* wave velocity depth function for the (left) 410-km and (right) 660-km discontinuities estimated from waveform inversion for earthquake 930921 and best waveform fitting model (solid line) and S8T9 (dashed line). Superimposed is the PPD (horizontal dashed lines) for the velocity parameters.

The PPDs curves are very broad for most of the velocity nodes, with the exception of the distribution at 655 km depth.

6.2. The Whole Data Set

Inversion of individual earthquake events provided us a set of slightly different velocity models for the transition zone. To obtain an average velocity for the region one could simply average the individual velocity models. Since the signal-to-noise ratio for individual events is generally low and the noise tends to map into velocity model, we have not averaged the individual models but instead simultaneously inverted the whole data for an average model. The best fitting velocity models for the 410- and 660-km upper mantle discontinuity are shown in Figure 8, and the seismograms computed from these models are shown in Figure 9. The waveform misfit of the best model for the entire suite of 36 seismograms was 0.683, which is a good numerical fit [*Sambridge and Drijkoningen*, 1992]. A misfit value close to zero is unrealistic given the presence of noise and unmodeled signal in the observed data. In Figure 9 one can see that the waveform match is fairly good. The synthetic seismograms obtained from the final velocity model for the 410-km discontinuity adequately fit the general features of the observed data. This improved fit is particularly apparent when these synthetic seismograms are compared to seismograms obtained from S8T9 for distances from 1400 to 2100 km.

7. Discussion

There are two possible sources of errors that could map into the final inversion results: (1) errors in source parameters and (2) 2-D effects. We have chosen events of moderate size so that the source parameters are simple. However, each of the events has different focal mechanisms. The errors in these parameters could be up to 20%. Interestingly enough, the inversion results for the individual events are very similar to that of all the events together for both the 410-km and 660-km discontinuities, suggesting that the effect of any errors in source parameters is not significant. The effect of 2-D crustal and upper mantle structures has been taken into consideration by using S8T9 model. As most of the arrivals considered here are critically reflected, any small-scale 2-D velocity variations in the upper part of the model would mainly effect the travel times, not the waveforms. However, it is possible that the region under investigation could have 2-D structure, which will smear out the final results. Since the inversion of individual events give similar results for all the events for both the 410-km and 660-km discontinuities, we could

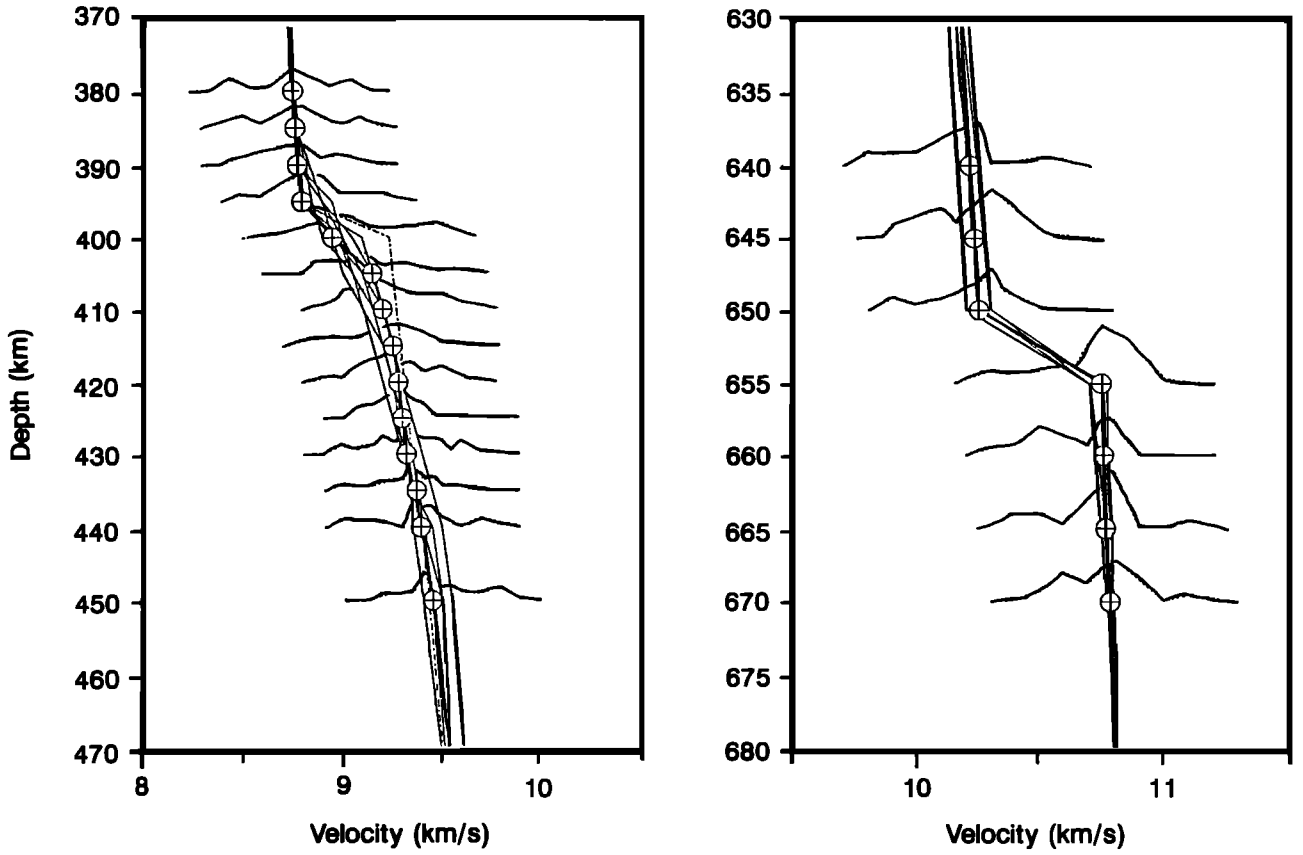

Figure 8. *P* wave velocity depth function for the (a, left) 410-km and (b, right) 660-km discontinuities from waveform inversion for individual and all earthquake events. Best waveform fitting model (thick solid line), individual events (thin solid lines), and S8T9 (dashed line). Superimposed is the PPD (horizontal dashed lines) for the velocity parameters.

assume that the velocity structures in the vicinity of these discontinuities are more or less one-dimensional.

7.1. The 410-km Discontinuity

Figure 8(left) shows that the estimated velocity models from individual earthquake events (thin solid lines) and from the whole data set (thick solid line with crossed circles) are quite similar. The overall differences in the estimated velocities are smaller than 0.2 km s^{-1}. Therefore the velocity model obtained from the inverting all the data set is a good representation of the individual events (but it is not an average model). Hence the final model for the discontinuity near the 410 km depth (Figure 8(left), thick solid line with crossed circles) consists of a one-stage velocity gradient. This gradient stage extends from 395 to 405 km depth, where the *P* wave velocity increases from 8.80 to 9.15 km s^{-1} (a gradient of 0.035 s^{-1}). We have assumed a constant travel time variance of $\sigma = 0.5$ s to evaluate the binned PPDs. Our velocity model is generally slower (up to 0.3 km s^{-1}) than S8T9. The synthetic seismograms obtained from the final velocity model for the 410-km discontinuity match the general features of the observed data better than those obtained from the S8T9. Our results indicate that the 410-km discontinuity beneath western United States is less sharp (thicker) than suggested by previous authors [*Burdick and Helmberger*, 1978; *Burdick*, 1981] but agrees with that of *Melbourne and Helmberger* [1998], who give a 14-km-thick transition under the southwestern United States.

A comparison of our results with three other models is shown in Figure 10. A model based on high-frequency precritical reflection data [*Vidale et al.*, 1995] shows that the 410-km discontinuity beneath Basin and Range province (dashed line) occurs over a depth range of <5 km. The IASP91 model [*Kennett and Engdahl*, 1991], which is based on travel time analysis, also suggests a sharp discontinuity. First, it is not possible to resolve structural features <5 km thick from travel time or waveform analysis of reflection data as the dominant frequency of the *P* wave in data is generally <2 Hz, giving a resolution of 5 km or more (for velocities between 9 and 10 km s^{-1}). Second, the high-pressure mineral physics data require α to β phase transition to take place over a range of 10-15 km [*Bina and Wood*, 1987; *Ita and Stixrude*, 1992; *Stixrude*, 1997]. Our 10-km-thick velocity gradient is able to explain the apparent disagreement between mineral physics and the above seismological observations. Our model is also consistent with the model derived by *Bowman and Kennett* [1990] from the analysis of broadband data beneath northwestern Australia (Figure 10, dotted line).

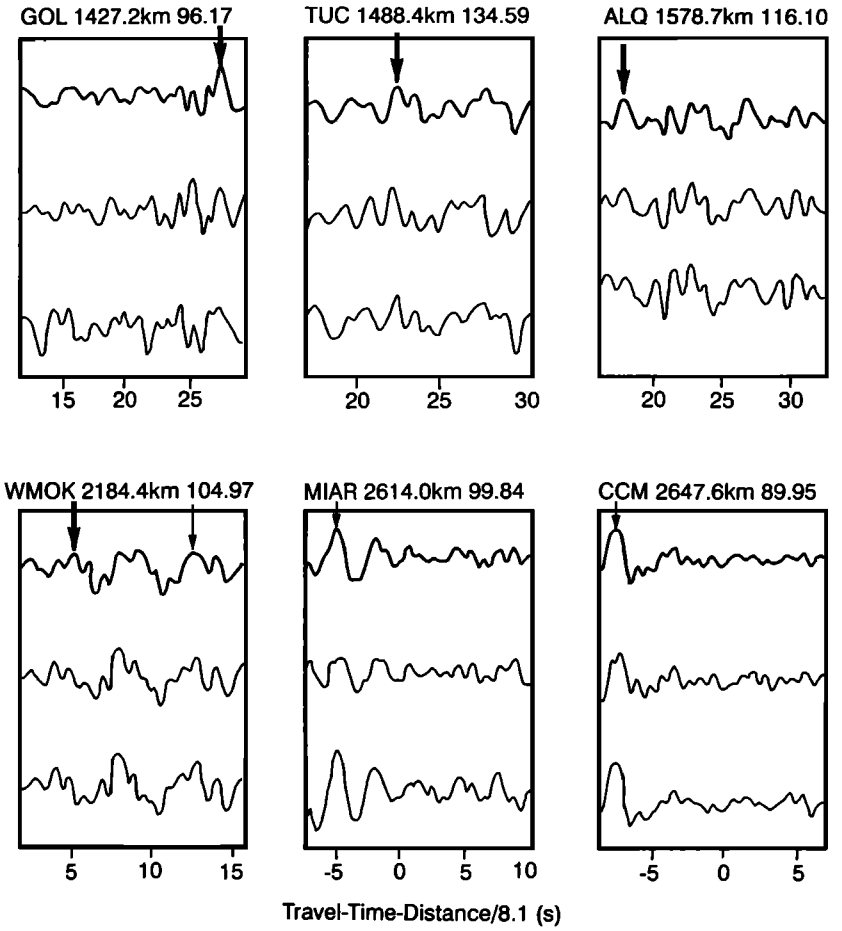

Figure 9. Comparison between the observed data (top curve) from the 930921 event and synthetic seismograms obtained from the best waveform fitting velocity model for all earthquake events (middle curve) and from S8T9 (bottom curve). The station name, distance, and azimuth are shown above each box. The source time function and the focal mechanism are shown in Figure 6. Arrivals from the 410- and 660-km discontinuities are identified by the thick and thin arrows, respectively.

7.2. The 660-km Discontinuity

The best waveform fitting models obtained from the inversion of the complete data set (thick solid line with crossed circles) and individual earthquake events (thin solid lines) for the 660-km discontinuity are shown in Figure 8(right). The velocity models derived from individual events (thin solid lines) and from all data (thick solid line) are very similar. The differences in the velocities are <0.1 km s^{-1}. Comparison between observed and synthetic waveforms (Figure 9) show that the main arrivals from the 660-km transition zone are well matched both in time and amplitude at all distances. The final model for the 660-km discontinuity obtained from inverting the whole data set (Figure 8(right), thick solid line) is also very similar to model S8T9 (Figure 8(right), dashed line). This transition zone is only 5 km thick, occurring over the depth range 650-655 km, where velocity ranges from 10.20 to 10.70 km s^{-1}. The PPDs functions for the 660-km discontinuity (Figure 8(right)) are less complex than the ones for the 410-km discontinuity (Figure 8(left)). This could be due to a simpler discontinuity structure, or a structure that is better constrained by this data set. The seismograms in Figure 9 show that the waveform match for stations within the distance range (2000-2600 km) for arrivals from the 660-km discontinuity is better fit than the arrivals in the distance range (1400-2100 km) for the 410-km discontinuity. The PPDs in Figure 8(right) show that the inverted velocity is well constrained with a velocity uncertainty of ± 0.25 km s^{-1}; however, several secondary optima occur (e.g., at 660 and 665 km depth for velocity between 10.30 and 10.40 km s^{-1}). This is a clear example of the importance of using a global inversion scheme that provides statistical assessment of the results. Forward modeling or local inverse methods could have been trapped within one of these local optima.

Figure 11 shows various velocity models that have been derived from previous earthquake studies. The solid line is the preferred velocity model of this study, the dashed line is the IASP91 model, and the dotted line is the NWB1 model. The first two models suggest a sharp velocity discontinuity of 5 km or less, while the third one is 20 km thick (from 610 to 630 km depth). Since our inversion results have an accuracy of ± 5 km,

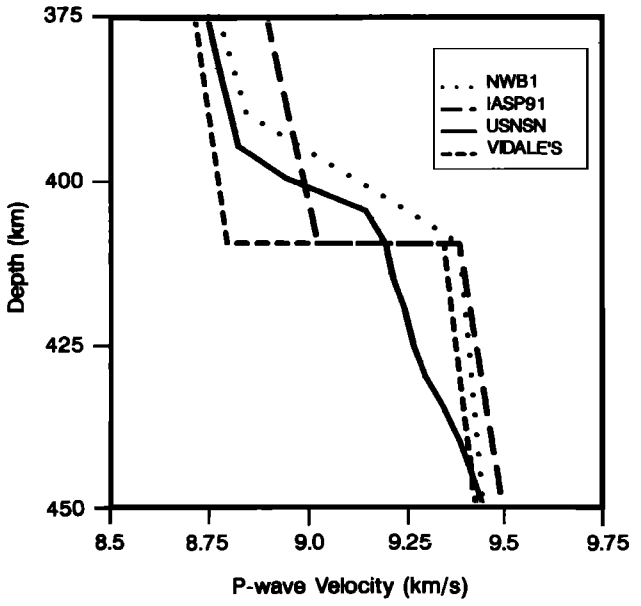

Figure 10. The P wave velocity depth function for the 410-km discontinuity estimated from inversion of the USNSN data set (solid line) is compared to average Earth model (IASP91 [*Kennett and Engdahl*, 1991]), northwestern Australia (NWB1 [*Bowman and Kennett*, 1990]) (dotted line), and northwestern North America [*Vidale et al.*, 1995] (long dashed line).

our velocity model and IASP91 are in agreement. There is no clear reason why our model does not agree with the NWB1 model. One obvious explanation is that the 660-km discontinuity is really broader and shallower beneath northern Australia.

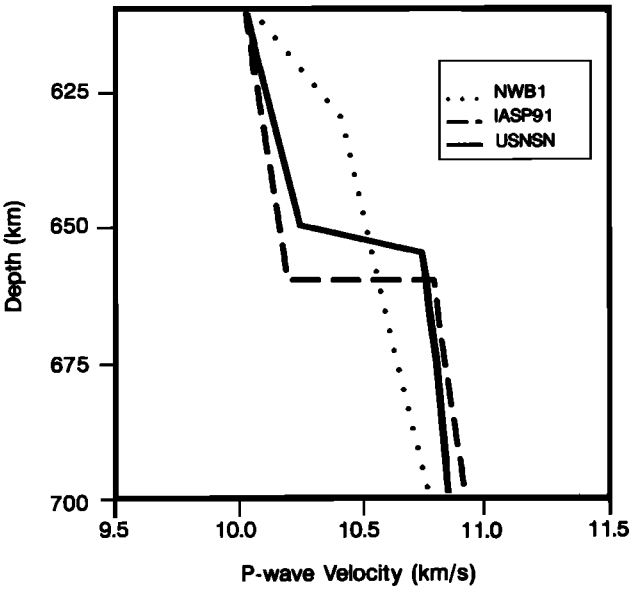

Figure 11. The P wave velocity depth function for the 660-km discontinuity estimated from inversion of the USNSN data set (solid line) compared to average Earth model (IASP91 [*Kennett and Engdahl*, 1991]) and northwestern Australia (NWB1 [*Bowman and Kennett*, 1990]) (dotted line).

8. Conclusions

We have developed a new method of waveform inversion and applied it to the study of the mantle transition zone beneath North America using broadband data seismic data. Our method provides a global solution to the inverse problem and uncertainty estimates for the final model. Our results suggest that the 410-km discontinuity is ~10 km thick and the 660-km discontinuity is 5 km thick, which is consistent with the results from the high-pressure mineral physics. The broader structure we find for the 410-km discontinuity cannot be a result of errors in our assumptions about the earthquake source since we would expect these type of errors to have a similar effect on the structure determined for both discontinuities. The similarity in the transition zone velocity models derived from fitting the individual waveforms and simultaneously fitting all waveforms suggests that there are no pronounced lateral variations in the transition zone structure beneath western North America.

Acknowledgments. We are grateful to Harley Benz for providing the USNSN data and to Don Helmberger and Sebastien Chevrot for constructive comments on the original manuscript. This is Cambridge University Department of Earth Sciences contribution 6490.

References

Akaogi, M., and E. Ito, Refinement of enthalpy measurement of $MgSiO_3$ perovskite and negative pressure-temperature slopes for perovskite forming reactions, *Geophys. Res. Lett.*, *20*, 1839–1842, 1993.

Akaogi, M., E. Ito, and A. Navrotsky, Olivine-modified spinel-spinel transitions in the system Mg_2SiO_4 – Fe_2SiO_4: Calorimetric measurements, thermochemical calculation, and geophysical application, *J. Geophys. Res.*, *94*, 15,671–15,685, 1989.

Basu, A., and L. N. Frazer, Rapid determination of the critical temperature in simulated annealing inversion, *Science*, *249*, 1409–1412, 1990.

Benz, H. M., and J. E. Vidale, Sharpness of upper mantle discontinuities determined from high-frequency reflections, *Nature*, *365*, 147–150, 1993.

Bina, C. R., and B. J. Wood, Olivine-spinel transitions: Experimental and thermodynamic constraints and implications for the nature of the 400-km seismic discontinuity, *J. Geophys. Res.*, *92*, 4853–4866, 1987.

Bowman, J. R., and B. L. N. Kennett, An investigation of the upper mantle beneath NW Australia using a hybrid seismograph array, *Geophys. J. Int.*, *101*, 411–424, 1990.

Burdick, L. J., A Comparison of the upper-mantle structure beneath North America and Europe, *J. Geophys. Res.*, *86*, 5926–5936, 1981.

Burdick, L. J., and D. V. Helmberger, The upper mantle P velocity structure of the western United States, *J. Geophys. Res.*, *83*, 1699–1712, 1978.

Cary, P. W., Waveform inversion of marine refraction data, Ph.D. dissertation, Univ. of Cambridge, Cambridge, England, 1988.

Cary, P. W., and C. H. Chapman, Automatic one-dimensional inversion of marine refraction data, *J. Geophys. Res.*, *93*, 527–546, 1988.

Červený, V., M. M. Popov, and I. Pšenčik, Computation of wave fields in inhomogeneous media-Gaussian beam ap-

proach, *Geophys. J. R. Astron. Soc., 70*, 109–128, 1982.

Chapman, C. H., The Earth flattening transformation in body wave theory, *Geophys. J. R. Astron. Soc., 35*, 55–70, 1973.

Chapman, C. H., and R. Drummond, Body-wave seismograms in inhomogeneous media using Maslov asymptotic theory, *Bull. Seismo. Soc. Am., 72*, S277–S317, 1982.

Dey, B. K., B. L. N. Kennett, J. R. Bowman, and A. Goody, Variations in upper mantle structure under northern Australia, *Geophys. J. Int., 114*, 304–310, 1993.

Frazer, L. N., and A. Basu, Freeze-bath inversion, paper presented at Sixtieth Annual International Meeting and Exposition, Soc. of Explor. Geophys., San Francisco, Calif., 1990.

Goldberg, D. E., *Genetic Algorithms in Search, Optimization and Machine Learning*, Addinson-Wesley-Longman, Reading, Mass., 1989.

Helffrich, G. R., and B. J. Wood, 410km discontinuity sharpness and the form of the olivine $\alpha - \beta$ phase diagram: Resolution of apparent seismic contradictions, *Geophys. J. Int., 126*, F7-F12, 1996.

Helmberger, D. V., Numerical seismograms of long period body waves, *Bull. Seismo. Soc. Am., 64*, 45-60, 1973.

Ita, J., and L. Stixrude, Petrology, elasticity, and composition of the mantle transition zone, *J. Geophys. Res., 97*, 6849–6866, 1992.

Katsura, T., and E. Ito, The system $Mg_2SiO_4 - Fe_2SiO_4$ at high-pressures and temperatures: Precise determination of stabilities of olivine, modified spinel, and spinel, *J. Geophys. Res., 94*, 15,663–15,670, 1989.

Kennett, B. L. N., and J. R. Bowman, The velocity structure and heterogeneity of the upper mantle, *Phys. Earth Planet. Inter., 59*, 134–144, 1990.

Kennett, B. L. N., and E. R. Engdahl, Travel-times for global earthquake location and phase identification, *Geophys. J. Int., 105*, 429–465, 1991.

Melbourne, T., and D. Helmberger, Fine structure of the 410-km discontinuity, *J. Geophys. Res., 103*, 10,091-10,102, 1998.

Nábělek, P., Determination of earthquake source parameters from inversion of body waves, Ph.D. thesis, Mass. Inst. of Technol., Cambridge, 1984.

Neves, F., Velocity structure of upper mantle discontinuities from global waveform inversion of wide-angle land seismic data, Ph.D. thesis, Univ. of Cambridge, Cambridge, England, 1996.

Neves, F., S. C. Singh, and K. Priestley, Velocity structure of the upper mantle transition zones beneath central Eurasia from seismic inversion using genetic algorithms, *Geophys. J. Int., 125*, 869–878, 1996.

Priestley, K., J. Cipar, A. Egorkin, and N. Pavlenkova, Upper-mantle velocity structure beneath the Siberian platform, *Geophys. J. Int., 118*, 369–378, 1994.

Sambridge, M. S., and G. G. Drijkoningen, Genetic Algorithms in seismic waveform inversion, *Geophys. J. Int., 109*, 323–342, 1992.

Sen, M. K., and P. L. Stoffa, Rapid sampling of model space using genetic algorithm: examples from seismic waveform inversion, *Geophys. J. Int., 108*, 281–292, 1992.

Shearer, P.C., Transition zone velocity gradients and the 520-km discontinuity, *J. Geophys. Res., 101*, 3053–3066, 1996.

Stixrude, L., Structure and sharpness of phase transitions and mantle discontinuities. *J. Geophys. Res., 102*, 14,835-14,852, 1997.

Vidale, J. E., X.-Y. Ding, and S. P. Grand, The 410-km-depth discontinuity: A sharpness estimate from near-critical reflections, *Geophys. Res. Lett., 22*, 2557–2560, 1995.

F.A. Neves and K. Priestley, Bullard Laboratories, Madingley Rise, Madingley Road, Cambridge CB30EZ, UK. (keith@esc.cam.ac.uk)

S.C. Singh, Laboratoire de Géosciences Marines, Institut de Physique du Globe de Paris, 4 Place Jussieu, 75252 Paris Cedex 05, France. (singh@ipgp.jussieu.fr)

(Received November 5, 1999; revised January 8, 2001; accepted April 25, 2001.)